Reversible Tuning of Superconductivity in Ion-Gated NbN Ultrathin Films by Self-Encapsulation with a High-κ Dielectric Layer

Erik Piatti,[1,†] Marco Colangelo,[2,†] Mattia Bartoli,[3,4] Owen Medeiros,[2] Renato S. Gonnelli,[1] Karl K. Berggren,[2] and Dario Daghero[1,*]

[1] *Department of Applied Science and Technology, Politecnico di Torino, Torino I-10129, Italy*

[2] *Department of Electrical Engineering and Computer Science, Massachusetts Institute of Technology, Cambridge, Massachusetts 02139, USA*

[3] *Center for Sustainable Future Technologies-CSFT@POLITO, Torino I-10144, Italy*

[4] *Consorzio Interuniversitario Nazionale per la Scienza e Tecnologia dei Materiali (INSTM), Firenze I-850121, Italy*

(Received 12 May 2022; revised 3 August 2022; accepted 19 September 2022; published 9 November 2022)

Ionic gating is a powerful technique for tuning the physical properties of a material via electric-field-induced charge doping, but is prone to introduce extrinsic disorder and undesired electrochemical modifications in the gated material beyond pure electrostatics. Conversely, reversible, volatile, and electrostatic modulation is pivotal in the reliable design and operation of novel device concepts enabled by the ultrahigh induced charge densities attainable via ionic gating. Here we demonstrate a simple and effective method to achieve reversible and volatile gating of surface-sensitive ultrathin niobium nitride films via controlled oxidation of their surface. The resulting niobium oxide encapsulation layer exhibits a capacitance comparable to that of nonencapsulated ionic transistors, withstands gate voltages beyond the electrochemical stability window of the gate electrolyte, and enables a fully reversible tunability of both the normal-state resistivity and the superconducting transition temperature of the encapsulated films. Our approach should be transferable to other materials and device geometries where more standard encapsulation techniques are not readily applicable.

DOI: 10.1103/PhysRevApplied.18.054023

I. INTRODUCTION

The ionic gating technique is a very powerful tool to tune the properties of a large variety of materials, including high-carrier density systems such as metals [1–6], BCS superconductors [7–11], thin flakes of metallic transition-metal dichalcogenides [12–14], and iron-based superconductors [15–21] using a field-effect transistor (FET) configuration. In principle, the basic mechanism by which it operates is electrostatic and fully reversible: when the interface between an electrolyte and the material under study is polarized by a gate voltage, the mobile ions accumulate in the so-called electric double layer (EDL) and build up electric fields about 100 times larger than those achievable in standard solid-dielectric FETs [22, 23]. In practice, however, many processes beyond pure electrostatics can occur in an EDL FET. These range from the introduction of extrinsic disorder in the form of charged scattering centers [21,24–32], to field-induced distortions in the crystal lattice [33–35], to the intercalation of alkali ions [36–46] or protons [47–54], to the outright electrochemical modification of the gated material [16, 33,34,55–62]. While these additional processes can be harnessed to provide additional degrees of freedom in modulating the properties of a material, it is often desirable to ensure that the modulation occurs only in the electrostatic regime. Indeed, reversible electrostatic switching is crucial for the realization of novel device concepts, such as chiral light-emitting transistors [63], superconducting (SC) FETs [64,65], nanoconstriction Josephson junctions [66,67], and metallic SC quantum interference devices [68], as well as for reliable operation of stretchable and flexible devices [69–71] and thermoelectric energy harvesters [72].

The most straightforward way to ensure that the operation of an EDL FET is dominated by reversible charge doping and that electrochemical interactions are suppressed is to physically separate the active material from the electrolyte using an electrically insulating and electrochemically inert layer. This can be achieved by employing an electrolyte that partially decomposes when polarized, creating a passivation layer [21], but this strongly reduces the switching speed of the device [21]. Another possibility is to employ encapsulation techniques widely used to protect unstable or reactive two-dimensional (2D)

*dario.daghero@polito.it

†These authors contributed equally.

materials in standard solid-state FETs [73]. For example, one can cover the surface of the active materials, prior to the exposition to the electrolyte, with a high-quality ultrathin layered insulator obtained by micromechanical exfoliation of a bulk crystal [13,14,24], or a protective dielectric layer [39,74]. These alternatives, however, can present drawbacks when used in a ionic-gating setup. For instance, the first approach is not easily scalable to multiple integrated devices and large-area geometries [13,14,24]. In the second approach, the thickness of the protective layer is critical: thick passivation films strongly suppress the gate capacitance [39,74], while thin uniform films cannot be deposited on several materials of interest [74]. The development of an alternative, complementary encapsulation technique is therefore highly desirable. In this work, we demonstrate that growth of an ultrathin high-κ dielectric layer on top of a surface-sensitive SC film by means of controlled *in situ* oxidation ensures a fully reversible operation of the EDL FET, a sizeable gate capacitance, a large induced charge-carrier density, and an enhanced tunability of the SC transition temperature with respect to the literature.

II. DEVICE FABRICATION

Our device consists of a niobium nitride multiple-Hall-bar structure. A 5-nm-thick niobium nitride (NbN) layer is deposited [75] on a 300-nm-thick thermal oxide layer on silicon. The NbN layer is patterned into a multiple-Hall-bar geometry (see Fig. 1) with direct-writing photolithography followed by reactive ion etching. To facilitate the electrical contact with the measurement wires, gold pads are patterned and deposited on the outer lead regions of the Hall bar. The device is then annealed in an oxygen atmosphere to grow a Nb_2O_5 insulating barrier via direct oxidation of the superconducting layer. The thickness of the oxide barrier is approximately 2.6 nm, measured with ellipsometry [76]. More details on the fabrication process are available in Sec. I of the Supplemental Material [77].

To characterize the device, we define two measurement channels. The active (gated) channel is created by drop casting the standard diethylmethyl (2-methoxyethyl) ammonium bis(trifluoromethylsulfonyl) imide (DEME-TFSI) ionic liquid on one section of the Hall bar and on the gate counterelectrode, made of a thin Au flake. The reference (ungated) channel is one of the other sections of the Hall bar, where no ionic liquid is casted. The droplet of liquid on the gated channel is covered with a thin (10 μm) kapton foil to tightly confine its coverage on the substrate and improve its thermomechanical stability.

III. GATE-DEPENDENT ELECTRIC TRANSPORT

Transport measurements are performed in the high-vacuum chamber of a Cryomech® pulse-tube cryocooler by the four-wire method after the device is allowed to degas in vacuum at room temperature for at least 1 day to minimize the water absorbed in the electrolyte. A small dc current (I_{DS}) of 1 μA is injected between the drain and source contacts with the first channel of an Agilent B2912 source-measure unit (SMU), and the voltage drops across the gated (V_{gated}) and reference (V_{ref}) channels are measured with two Agilent 34420 nanovoltmeters to determine the corresponding sheet resistances (R_s). Common-mode offsets such as thermoelectric voltages along the leads and contributions from the gate current are removed via the current-reversal method. The gate voltage (V_G) and current (I_G) are applied and measured between the gate and source contacts with the second channel of the same Agilent SMU. All the temperature- (T) dependent measurements are acquired during the slow, quasistatic warm-up of the devices to room temperature.

We first assess the gate-dependent electric transport in our EDL FETs through the Nb_2O_5 encapsulation layer by sweeping V_G in a triangular wave at $T = 220$ K and monitoring the modulation of the sheet resistance R_s [Fig. 2(a)]. Consistently with what we observe in thick, nonencapsulated films [9,10], applying a positive V_G (electron doping) reduces the value of R_s, while applying a negative V_G (hole doping) increases it. After completing each sweep,

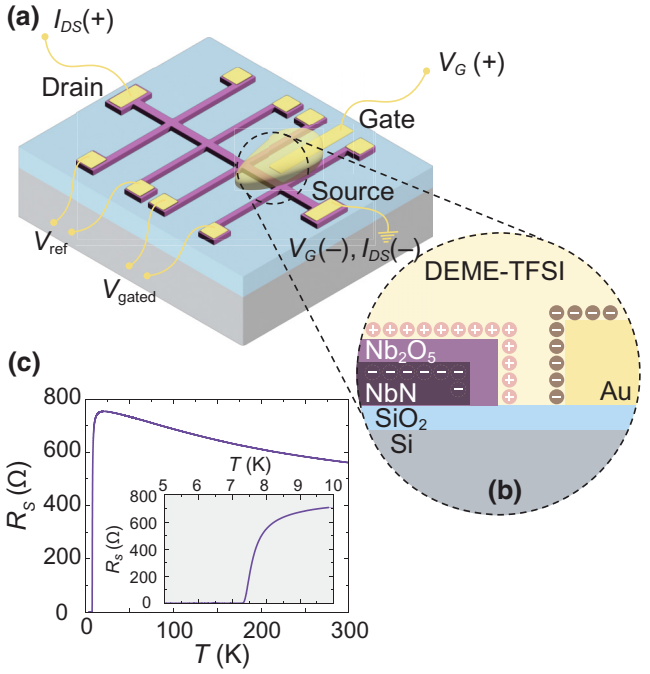

FIG. 1. (a) Sketch of the multiple-Hall-bar structure and of the measurement configuration. Each channel is 1.15 mm long and 100 μm wide. The typical size of the Au side gate is 0.8×1.2 mm^2. The ionic liquid droplet is drop casted so as to cover the Au gate and the gated channel only. (b) Sketch of the cross section of the gated channel. (c) Sheet resistance R_s as a function of temperature T of the reference channel. Inset shows a magnification around the superconducting transition.

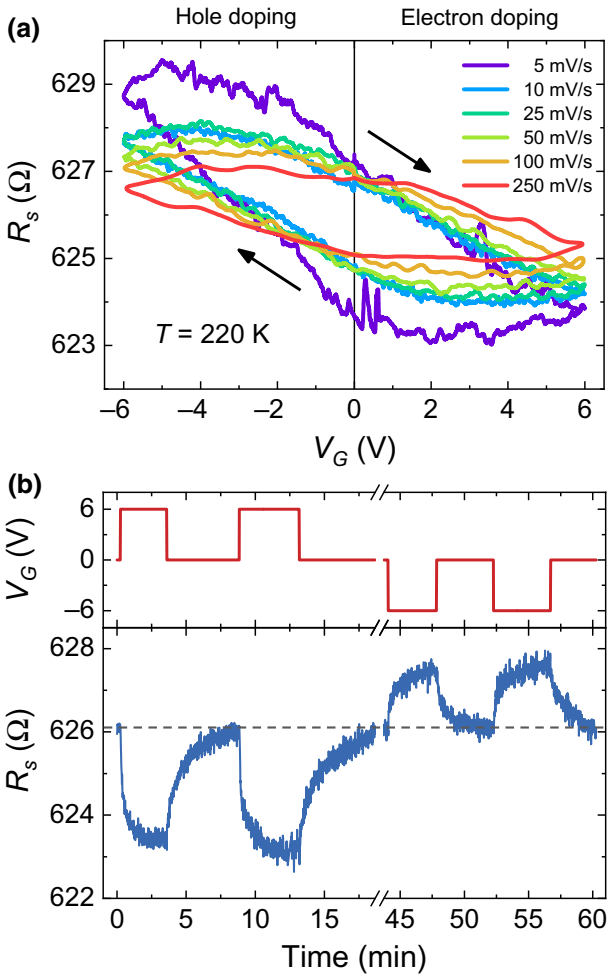

FIG. 2. (a) Sheet resistance R_s as a function of the gate voltage V_G applied as a triangular wave at $T = 220$ K for different values of the sweep rate. (b) Typical response of R_s (blue line, bottom panel) to the steplike application and removal of positive and negative values of V_G (red line, top panel) at $T = 220$ K. Dashed line is a guide to the eye.

R_s returns to its original value (Fig. S1 within the Supplemental Material [77]) irrespectively of the sweep rate within the uncertainty of the measurement. The leakage current I_G is always orders of magnitude smaller than I_{DS}. The tunability of R_s decreases upon increasing the sweep rate, indicating that the relaxation time of the gate loop is dominated by the large resistance of the bulk ionic liquid due to the side-gate configuration [21,78]. We thus investigate the tunability of R_s over long time scales by applying and removing V_G in a steplike fashion and waiting for the ion dynamics to settle [Fig. 2(b)]. The total modulation of R_s is found to be similar to that due to the triangular wave at the slowest sweep rate 5 mV/s. Most importantly, the modulation is completely reversible upon applying $V_G = 0$ over a comparable time scale to that required for the saturation of R_s upon application of a finite V_G. This complete reversibility is observed for both positive and negative applied V_G in the Nb_2O_5-encapsulated devices, which is the typical feature of a modulation occurring via pure charge doping [1,2,21,30]. Note that these reversible modulations of R_s are retained when the devices are then cooled below the freezing point of the ionic liquid with a finite V_G applied (Fig. S2 within the Supplemental Material [77]), further excluding the possibility that they might be an artifact due to a finite (even if small) gate leakage. Conversely, control measurements performed on nonencapsulated ultrathin NbN films result in modulations of R_s that are largely irreversible upon V_G removal (Fig. S3 within the Supplemental Material [77]). This finding is in agreement with our earlier results on nonencapsulated films when their thickness was reduced below about 10 nm [10].

We gain further insight on the gate modulation process in our encapsulated NbN films by determining the surface density of induced charge, Δn_{2D}, as a function of V_G. This can be done by means of double-step chronocoulometry, a well-established electrochemical technique [79] that allows determining the charge density stored in the EDL during the FET charging process [1,2,9,10,21,30,32] through the analysis of the I_G transients upon the steplike application and removal of a given value of V_G. As we show in the inset to Fig. 3, the V_G dependence of Δn_{2D} further demonstrates that gate modulation occurs

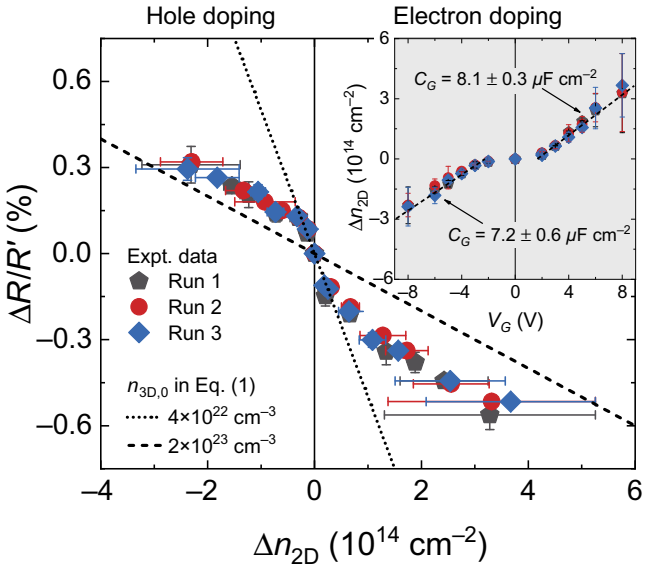

FIG. 3. Normalized resistance variation, $\Delta R/R' = [R_s(\Delta n_{2D}) - R_s(0)]/R_s(\Delta n_{2D})$ as a function of the induced charge density Δn_{2D} obtained upon the steplike application of V_G. Inset: the induced charge density Δn_{2D} as a function of the applied gate voltage V_G determined via double-step chronocoulometry in the same measurements. Dashed lines are linear fits to the data and allow us to estimate the gate capacitance C_G.

via charge doping: Δn_{2D} linearly increases upon increasing V_G for both electron and hole doping, as expected for the electrostatic charging of a capacitor. The corresponding gate capacitances ($C_G = 8.1 \pm 0.3$ and $7.2 \pm 0.6\ \mu\mathrm{F\,cm^{-2}}$ as estimated from the linear fits in the electron and hole doping regimes, respectively) are also in agreement with a simple estimation of the electrostatic capacitance of a Nb_2O_5 layer with permittivity $\varepsilon_r \sim 30$ [80] and thickness $d_{ox} \simeq 3$ nm, $C_{ox} = \varepsilon_r \varepsilon_0 / d_{ox} \simeq 8.8\ \mu\mathrm{F\,cm^{-2}}$.

Let us now consider the normalized resistance modulation $\Delta R/R' = [R_s(\Delta n_{2D}) - R_s(0)]/R_s(\Delta n_{2D})$ as a function of the induced charge density Δn_{2D} (Fig. 3). This quantity clearly follows two distinct linear trends (highlighted by the straight dashed and dotted lines) in the low- and high-Δn_{2D} regimes. For the sake of comparison, in gated homogeneous films of elemental metals (Au, Ag, Cu) [1,2], $\Delta R/R'$ displays a simple linear trend, with the same slope in the whole range of Δn_{2D}, that can be described by a simple free-electron model with constant effective mass and relaxation time [1,2,21]. The model predicts that $\Delta R/R'$ should depend on Δn_{2D} according to the equation

$$\frac{\Delta R}{R'} = \frac{R_s(\Delta n_{2D}) - R_s(0)}{R_s(\Delta n_{2D})} = -\frac{\Delta n_{2D}}{n_{3D,0} t}, \tag{1}$$

where $n_{3D,0}$ is the intrinsic carrier density per unit volume and t is the film thickness. Deviations from this trend, with a reduction of the slope, were observed at high gate voltages in ultrathin metallic films ($t \simeq 5$ nm) [1,2] and were ascribed to scattering phenomena at the film surface, which are not accounted for by Eq. (1) but play a role when the thickness becomes comparable to the mean free path, as well predicted by quantum perturbative scattering models.

In our NbN films, the departure of the data from the initial linear trend cannot be interpreted in the same way, since: (i) the mean free path of NbN is known to be very small (approximately 1/10 of the film thickness) so that these films are actually bulklike [81]; (ii) if one uses the thickness of the films $t = 5$ nm, it turns out that the intrinsic carrier density of NbN $n_{3D,0} \simeq 2 \times 10^{23}\ \mathrm{cm^{-3}}$ [82] would be compatible with the *high-doping* slope $\Delta R/R'$ (see the dashed line in Fig. 3) rather than with the low-doping one, which would instead correspond to $n_{3D,0} \simeq 4 \times 10^{22}\ \mathrm{cm^{-3}}$ (dotted line). This indicates that, in the low-V_G regime, the resistance modulation mainly stems from the charge doping of a layer that is less conducting than NbN. This conclusion is supported by the compositional analysis of the films (see the x-ray photoelectron spectroscopy analyses below) that evidences the existence of an intermediate interfacial layer of the suboxide species NbO_xN_{1-x} between the NbN film and the Nb_2O_5 oxide layer. At low gate voltages, this layer is less conductive and less capacitive than NbN [82,83], absorbs most of the voltage drop through the device and is thus preferentially charge doped. Eventually, on increasing the gate voltage, its charge density may become similar to that of NbN and the charge induction into the whole NbN film dominates. A more detailed analysis of the $\Delta R/R'$ trend, that takes into account the existence of *two* layers of different materials, is reported in Sec. V of the Supplemental Material [77].

Incidentally, Fig. 3 also shows that the Nb_2O_5 encapsulation allows safely operating the EDL FET beyond the electrochemical stability window of the ionic liquid ($|V_G| \leq 6$ V at $T \sim 220$ K): all the resistance modulations induced at $V_G = \pm 8$ V (that correspond to $|\Delta n_{2D}| \gtrsim 2 \times 10^{14}\ \mathrm{cm^{-2}}$; see the inset) extrapolate nicely to the linear scaling observed at lower doping levels and the relevant resistance modulations remain reversible—even though a large uncertainty is introduced in the determination of Δn_{2D} due to the large increase in I_G caused by the decomposition of the ionic liquid.

We now consider how the ionic gate modulates the SC properties of our encapsulated NbN ultrathin films, focusing on the dependence of the SC transition temperature T_c on Δn_{2D}. Since the gate-induced T_c shifts can be as small as a few millikelvin, we adopt a differential technique allowed by the simultaneous measurements of the resistive transition in the active (T_c^{act}) and reference (T_c^{ref}) channels [9,10,21]: for each threshold $\tau = 10, 50, 90$ [i.e., 10, 50, and 90% of the resistive transition; see Fig. 4(a)], the T_c shift due to the application of a certain value of V_G is determined as

$$\Delta {T_c}^{\tau}(V_G) = [{T_c}^{\tau,act} - {T_c}^{\tau,ref}]_{V_G} - [{T_c}^{\tau,act} - {T_c}^{\tau,ref}]_0. \tag{2}$$

We also define a relative temperature scale T^* whose zero falls on the midpoint (50%) of the transition in the reference channel. As a matter of fact, resistance versus temperature curves at different values of V_G are necessarily recorded in different runs, since the gate voltage can be changed only at high temperature (> 200 K), i.e., above the freezing point of the ionic liquid. Therefore, even the R versus T curves of the ungated channel may not fall exactly on top of one another, due to a small thermal hysteresis. This does not affect in any way the determination of the T_c shift due to charge accumulation, but may generate confusion when R versus T curves measured at different V_G are plotted in the same graph. To avoid this problem and improve the readability of the graphs, we use T^*, defined as [9,10,21]

$$T^* = [T - {T_c}^{50,ref}]_{V_G} - [{T_c}^{50,act} - {T_c}^{50,ref}]_0. \tag{3}$$

The application of positive values of V_G (electron doping) shifts the resistive transition to lower temperatures, while that of negative values of V_G (hole doping) shifts it to higher temperatures [Fig. 4(a)], consistently with what

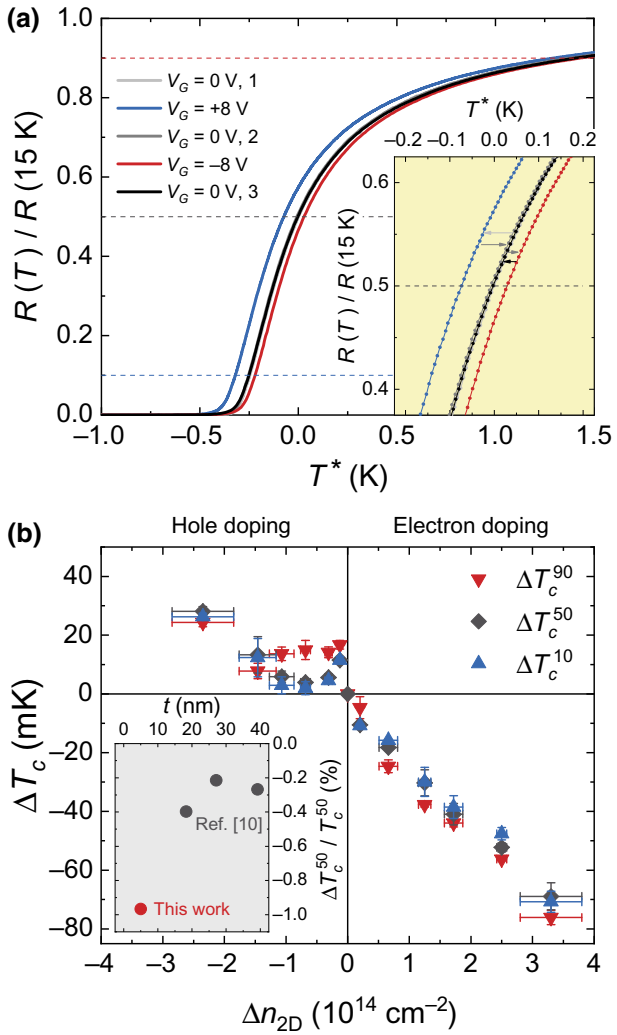

FIG. 4. (a) Normalized resistance $R/R(15\ \mathrm{K})$ as a function of the referenced temperature $T^* = [T - T_c^{\mathrm{ref}}]_{V_G} - [T_c^{\mathrm{act}} - T_c^{\mathrm{ref}}]_0$ for different values of the applied gate voltage V_G. Dashed lines highlight the criteria used to obtain T_c^{10}, T_c^{50}, and T_c^{90} from the resistive transitions. Inset: enlargement of the same data close to the midpoint of the transition (T_c^{50}). (b) The T_c shift ΔT_c as a function of the induced charge density Δn_{2D} determined for T_c^{10} (blue up triangles), T_c^{50} (black diamonds), and T_c^{90} (red down triangles). Inset: maximum T_c tunability $\Delta T_c^{50}/T_c^{50}$ as a function of the NbN film thickness. Black dots are calculated from the data of Ref. [10]. The red dot is the maximum tunability achieved in this work.

was reported on thick NbN films [7,9,10]. Similarly to the R_s modulations, the shifts in the resistive transition are also fully reversible by simply removing the applied V_G, as shown in the inset to Fig. 4(a). This reversible behavior must be compared with the control measurements performed on ultrathin nonencapsulated films, where the T_c suppression upon electron doping is only partially reversible (Fig. S4a in the Supplemental Material [77]), and—most importantly—hole doping not only does not increase T_c but suppresses it in a *completely irreversible* fashion (Fig. S4b in the Supplemental Material [77]). Notably, the Nb_2O_5 encapsulation allows for this fully reversible behavior to be maintained even for values of V_G in excess of the electrochemical stability window of the ionic liquid (at least up to $V_G = \pm 8$ V), while in nonencapsulated films much smaller values of V_G are sufficient to trigger irreversible modifications—again, consistent with how irreversible T_c shifts were induced in nonencapsulated NbN films when their thickness was reduced below about 10 nm in our earlier report [10].

In Fig. 4(b) we summarize all the T_c shifts measured as a function of Δn_{2D} in our encapsulated films. In the *electron doping* regime, T_c is monotonically suppressed in a nearly linear fashion on increasing Δn_{2D}. Moreover, the T_c shifts are nearly independent of the criterion used to define T_c, i.e., on the threshold τ, which indicates that the resistive transition is rigidly shifted by the charge doping without any appreciable broadening. This is an expected feature for a gated SC film with a thickness smaller than the coherence length [7,10,84,85], since the proximity effect "spreads" the perturbation to the SC order parameter well beyond its electrostatic screening length [7,10,86] and potentially up to the London penetration depth [65].

In the *hole doping* regime, things are more complicated. The T_c enhancement is found to be almost independent of τ only at large $\Delta n_{2D} \lesssim -2 \times 10^{14}$ cm^{-2}. At smaller hole doping, ΔT_c^{90} turns out to be nearly doping independent, but ΔT_c^{50} and ΔT_c^{10} vary in a nonmonotonic fashion as a function of Δn_{2D} and, although always positive, are smaller than ΔT_c^{90}. This indicates a broadening of the SC transition that is instead typically observed in films where the SC order parameter is perturbed in a nonhomogeneous way [21,65]. Overall, this asymmetric tuning of T_c has already been observed in thicker, nonencapsulated NbN films [9,10] and can be ascribed to the similarly asymmetric energy dependence of the density of states above and below the undoped Fermi level.

Another figure of merit of our encapsulated ultrathin films is the maximum T_c tunability, defined as the maximum value of $|\Delta T_c^{50}|/T_c^{50}$ observed in a given film. If compared to previous results obtained in thicker NbN films [10], the maximum tunability achieved in these ultrathin films is nearly 3 times larger and approaches 1% [see the inset to Fig. 4(b)]. Notably, this strongly improved tunability is obtained at much lower values of charge doping: $\Delta T_c^{50} \approx -70$ mK is obtained at $\Delta n_{2D} \simeq 3 \times 10^{14}$ cm^{-2} in ultrathin encapsulated films, whereas the same T_c shift required attaining $\Delta n_{2D} > 1 \times 10^{15}$ cm^{-2} in about 10-nm-thick nonencapsulated films in Ref. [10]. Further large improvements can be expected by properly optimizing the growth process of the Nb_2O_5 encapsulation layer and increasing its relative permittivity up to $\varepsilon_r \sim 90$ [80].

IV. SPECTROSCOPIC CHARACTERIZATION OF THE GATE INTERFACE

As a further support of the effectiveness of the Nb_2O_5 encapsulation layer in ensuring an electrostatic operation of the gated NbN devices, we carry out detailed analyses by means of x-ray photoelectron spectroscopy (XPS). Following a similar protocol as in our previous work [21], three unpatterned films are covered by DEME-TFSI ionic liquid and loaded in the cryocooler with the same procedure as the patterned devices. The first film is not electrically contacted and serves as the pristine reference. The other two films are electrically contacted and subjected to $V_G = +6$ and -6 V at $T = 220$ K, respectively, for about 30 min. All the films are then cooled down to the base temperature and warmed up, after which V_G is released in the gated films. All films are then cleaned by subsequent sonications in soapy water, acetone, and ethanol (about 30 min each; the procedure is safe against modifications of the physical and chemical states of the inorganic components [87,88]) and blow dried with a nitrogen gun, after which they are immediately transferred to the ultrahigh vacuum chamber of a PHI 5000 Versaprobe scanning x-ray photoelectron spectrometer. XPS spectra are acquired using a monochromatic Al K-alpha x-ray source with 1486.6-eV energy, 15-kV voltage, and 1-mA anode current. Despite the cleaning process, the survey spectra of all samples (Fig. S6 in the Supplemental Material [77]) show a massive presence of carbon contamination, which is unavoidable since ultrathin samples cannot be subjected to *in situ* Ar-ion milling before the acquisition of the XPS spectra [21]. Such presence of organic species with unknown stoichiometry makes an unambiguous peak assignment of the N and O signals impossible, making their analysis highly speculative at best. We therefore focus on the high-resolution Nb3*d* spectra shown in Fig. 5, which are unaffected by impurities and ionic-liquid residues, and highly sensitive to the chemical environment in both the Nb_2O_5 encapsulation layer and the underlying NbN film. The spectrum of the pristine sample [Fig. 5(a)] comprises two peaks belonging to NbN ($3d_{5/2}$, about 203.8 eV; $3d_{3/2}$, about 205.1 eV) [89,90], two peaks due to the massive presence of Nb_2O_5 ($3d_{5/2}$, about 206.9 eV; $3d_{3/2}$, about 209.5 eV) [89,90], and a fifth peak centered at about 208.2 eV that can be reasonably assigned to the intermediate suboxide species NbO_xN_{1-x} [91]. This suggests that, even in the pristine sample, the Nb_2O_5 and NbN layers are not separated by a sharp interface but, rather, by an intermediate transition region formed by substoichiometric niobium oxynitride. The spectra of both the gated samples [Fig. 5(b), $V_G = +6$ V; Fig. 5(c), $V_G = -6$ V] do not show any appreciable difference with respect to the pristine sample in the Nb_2O_5 peaks, as evidenced by the peak areas reported in Table I. Minute differences $\lesssim 2\%$ are instead observed in the NbN peaks and in the NbO_xN_{1-x} peak, which are

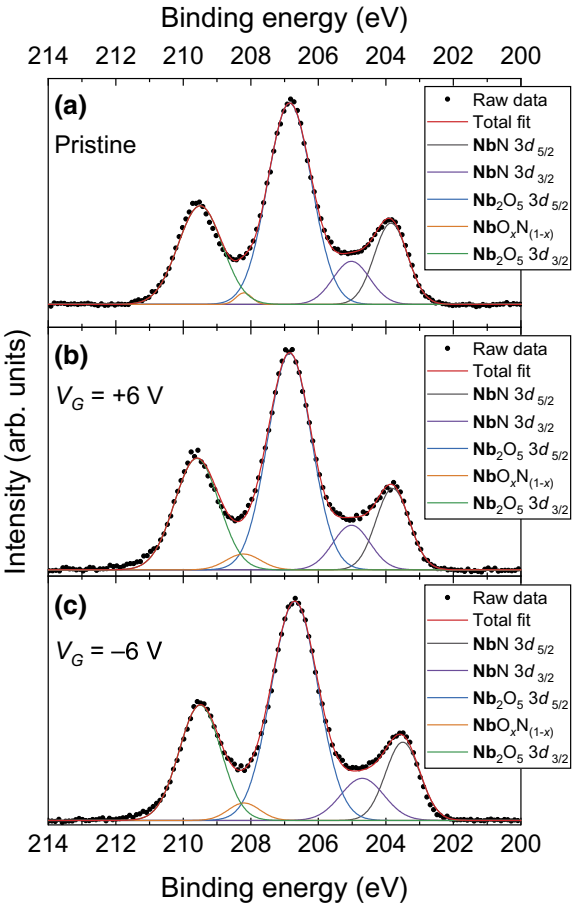

FIG. 5. High-resolution x-ray photoelectron spectroscopy spectra of the Nb3*d* region in (a) an ungated NbN film, (b) a NbN film gated at $V_G = +6$ V, and (c) a NbN film gated at $V_G = -6$ V. Filled circles are the experimental data; solid lines are the fitted signals and relative components.

however extremely sensitive to both fitting procedure and baseline correction. Overall, the XPS analysis indicates that the thickness of the oxynitride transition region might be significantly increased by the gating process, certainly at the expenses of both the NbN film and the Nb_2O_5 encapsulation layer, even though the reduction in the thickness of the latter is, in percentage, very small and experimentally undetectable. Any change to the electronic properties

TABLE I. XPS peak ratios of the Nb3*d* region in a pristine NbN film, a NbN film gated at $V_G = +6$ V, and a NbN film gated at $V_G = -6$ V.

Species	Pristine (atom %)	Gated +6 V (atom %)	Gated −6 V (atom %)
NbN	24.2 ± 0.7	22.6 ± 0.7	22.4 ± 0.4
Nb_2O_5	74.6 ± 0.7	74.6 ± 0.6	74.9 ± 0.6
NbO_xN_{1-x}	1.0 ± 0.2	2.8 ± 0.4	2.7 ± 0.6

of either the Nb_2O_5 or the NbN layers is instead completely volatile upon removal of the gate voltage.

The increase of the oxynitride transition region and the consequent change in the mean potential barrier of the encapsulation layer is also confirmed by tunnel spectroscopy through the Nb_2O_5 barrier. After a set of ionic gating measurements, we clean the surface of the devices and make point contacts (with a conductive Ag paste) on top of either the active (gated) channel or the reference (ungated) channel. A picture of the setup is shown in the inset to Fig. 6(a). We then inject a current I into the $Ag/Nb_2O_5/NbN$ junctions and measure the voltage drop $V^+ - V^- = V_{exp}$ both in the superconductive and in the normal state. This is done in order to determine and cancel the contribution of the spreading resistance r_s (i.e., the portion of NbN film between the point contact and the V^- contact) to the measured $I(V_{exp})$ curve. Once the measured voltage is suitably corrected $[V(I) = V_{exp}(I) - r_s I]$, we determine the $I(V)$ curve of each junction in the normal state. Figure 6(a) reports two examples of such curves, measured on the reference channel (blue symbols) and on the active one (red symbols). Clearly, the latter shows a greater degree of nonlinearity that, once the curves are fitted to the simple Simmons' model [92], can be rationalized as being due to a higher thickness and smaller height of the potential barrier that separates the normal electrodes (see Sec. VII of the Supplemental Material for more details [77]). As shown in Figs. 6(b) and 6(c), this is a general trend; the mean height of the potential barrier is $\langle\phi\rangle_u = 0.60 \pm 0.13$ V before gating, and decreases to $\langle\phi\rangle_g = 0.39 \pm 0.07$ V after gating; at the same time, the thickness of the potential barrier increases from $\langle s\rangle_u = 2.62 \pm 0.33$ nm to $\langle s\rangle_g = 3.34 \pm 0.34$ nm. Both these results are compatible with the expansion (by a factor of 3; see the last line of Table I) of the intermediate interfacial layer of substoichiometric oxide, as observed via XPS, at the expenses of the NbN film and possibly of the Nb_2O_5 encapsulation layer—provided that one admits, as seems reasonable, that the relevant potential barrier is lower than that of the insulating oxide. A rough estimation based on the XPS and tunnel data would indicate that the interfacial layer has a thickness of the order of 0.3 nm in the ungated devices, and expands to about 1 nm in the gated ones. A schematic picture of the junction is shown in Figs. 6(d) and 6(e) in the ungated and gated devices, respectively.

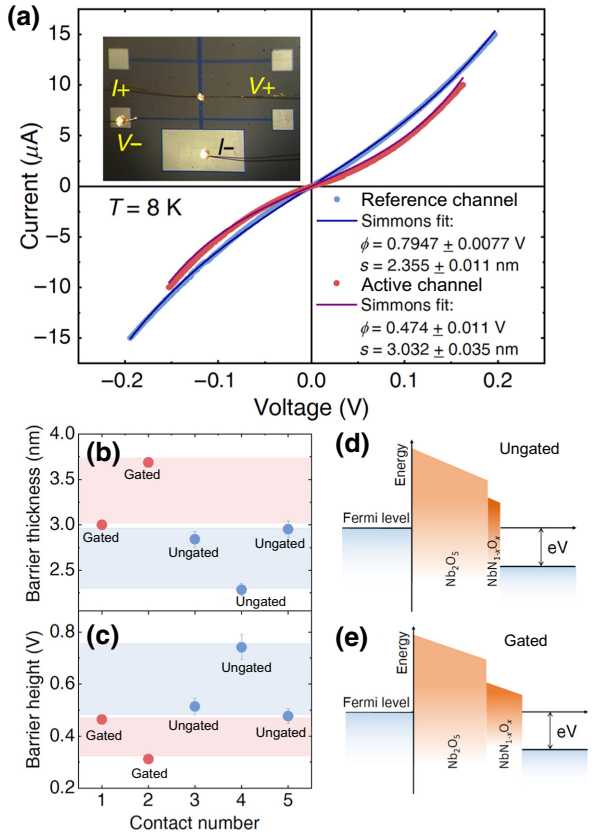

FIG. 6. (a) Two examples of $I(V)$ characteristics of N/I/N junctions made through the Nb oxide layer, in a region of the reference channel (blue symbols) and in a region of the active channel (red symbols). The curves have already been corrected to eliminate the contribution of the spreading resistance. The blue and the red lines represent their fit with the Simmons model [92]. The values of ϕ (barrier height) and s (barrier thickness) extracted from the fit are indicated. For these particular fits, the area of the junctions is fixed to 1.2×10^{-8} m, based on the geometric estimation. The inset shows a picture of the setup. (b) Effective thickness s and (c) effective height ϕ of the potential barrier, as extracted from the Simmon's fit of some $I(V)$ curves in the ungated (blue symbols) and gated (red symbols) channels. Panels (d) and (e) summarize in a schematic picture the evolution of the potential barrier upon gating, as it results from XPS and tunnel measurements.

V. CONCLUSIONS

In summary, we have demonstrated a simple and effective method to ensure the volatile and reversible operation of ion-gated superconducting films by means of encapsulation in an ultrathin high-κ dielectric niobium oxide layer. Our gate-dependent electric transport measurements show that encapsulated devices exhibit fully reversible tunability of both the normal-state resistivity and the superconducting transition temperature, a gate capacitance comparable to that found in nonencapsulated ionic transistors, and stability even beyond the electrochemical stability window of the electrolyte. X-ray photoelectron and tunnel spectroscopy characterizations confirm the effectiveness of the encapsulation layer in suppressing undesired electrochemical interactions between the superconducting film and the electrolyte, and reveal how the only nonvolatile alteration to the devices is an increase in the thickness of the substoichiometric interfacial region between the superconducting film and the encapsulation layer. Our approach should be readily transferable to other materials and devices where

ensuring a reversible and volatile ionic gate operation without major losses in gate capacitance is required for successful device operation.

ACKNOWLEDGMENTS

We thank S. Guastella and F. Galanti for assistance in the XPS and transport measurements, respectively. We thanks J. Daley and M. K. Mondol of the MIT Nanostructures Laboratory Facility for technical support. We thank E. Batson for assistance in editing the final manuscript. E.P., D.D., and R.S.G. acknowledge funding from the Italian Ministry of Education, University and Research (Project PRIN "Quantum2D", Grant No. 2017Z8TS5B). M.C., O.M., and K.K.B. acknowledge funding from the National Science Foundation under Grant No. ECCS-2000743. M.C. acknowledges support from the Claude E. Shannon Award.

[1] D. Daghero, F. Paolucci, A. Sola, M. Tortello, G. A. Ummarino, M. Agosto, R. S. Gonnelli, J. R. Nair, and C. Gerbaldi, Large Conductance Modulation of Gold Thin Films by Huge Charge Injection via Electrochemical Gating, Phys. Rev. Lett. **108**, 066807 (2012).

[2] M. Tortello, A. Sola, K. Sharda, F. Paolucci, J. R. Nair, C. Gerbaldi, D. Daghero, and R. S. Gonnelli, Huge field-effect surface charge injection and conductance modulation in metallic thin films by electrochemical gating, Appl. Surf. Sci. **269**, 17 (2013).

[3] S. Shimizu, K. S. Takahashi, T. Hatano, M. Kawasaki, Y. Tokura, and Y. Iwasa, Electrically Tunable Anomalous Hall Effect in Pt Thin Films, Phys. Rev. Lett. **111**, 216803 (2013).

[4] S. Dushenko, M. Hokazono, K. Nakamura, Y. Ando, T. Shinjo, and M. Shiraishi, Tunable inverse spin Hall effect in nanometer-thick platinum films by ionic gating, Nat. Commun. **9**, 3118 (2018).

[5] L. Liang, Q. Chen, J. Lu, W. Talsma, J. Shan, G. R. Blake, T. T. Palstra, and J. Ye, Inducing ferromagnetism and Kondo effect in platinum by paramagnetic ionic gating, Sci. Adv. **4**, eaar2030 (2018).

[6] L. Liang, J. Shan, Q. Chen, J. Lu, G. R. Blake, T. T. Palstra, G. E. Bauer, B. Van Wees, and J. Ye, Gate-controlled magnetoresistance of a paramagnetic-insulator—platinum interface, Phys. Rev. B **98**, 134402 (2018).

[7] E. Piatti, Ionic gating in metallic superconductors: A brief review, Nano Ex. **2**, 024003 (2021).

[8] J. Choi, R. Pradheesh, H. Kim, H. Im, Y. Chong, and D.-H. Chae, Electrical modulation of superconducting critical temperature in liquid-gated thin niobium films, Appl. Phys. Lett. **105**, 012601 (2014).

[9] E. Piatti, A. Sola, D. Daghero, G. A. Ummarino, F. Laviano, J. R. Nair, C. Gerbaldi, R. Cristiano, A. Casaburi, and R. S. Gonnelli, Superconducting transition temperature modulation in NbN via EDL gating, J. Supercond. Novel Magn. **29**, 587 (2016).

[10] E. Piatti, D. Daghero, G. A. Ummarino, F. Laviano, J. R. Nair, R. Cristiano, A. Casaburi, C. Portesi, A. Sola, and R. S. Gonnelli, Control of bulk superconductivity in a BCS superconductor by surface charge doping via electrochemical gating, Phys. Rev. B **95**, 140501(R) (2017).

[11] F. Paolucci, F. Crisá, G. De Simoni, L. Bours, C. Puglia, E. Strambini, S. Roddaro, and F. Giazotto, Electrostatic field-driven supercurrent suppression in ionic-gated metallic superconducting nanotransistors, Nano Lett. **21**, 10309 (2021).

[12] M. Yoshida, J. Ye, T. Nishizaki, N. Kobayashi, and Y. Iwasa, Electrostatic and electrochemical tuning of superconductivity in two-dimensional $NbSe_2$ crystals, Appl. Phys. Lett. **108**, 202602 (2016).

[13] L. J. Li, E. C. T. O'Farrell, K. P. Loh, G. Eda, B. Özyilmaz, and A. H. Castro Neto, Controlling many-body states by the electric-field effect in a two-dimensional material, Nature **529**, 185 (2016).

[14] X. Xi, H. Berger, L. Forró, J. Shan, and K. F. Mak, Gate Tuning of Electronic Phase Transitions in Two-Dimensional $NbSe_2$, Phys. Rev. Lett. **117**, 106801 (2016).

[15] C. Zhu, J. Cui, B. Lei, N. Wang, C. Shang, F. Meng, L. Ma, X. Luo, T. Wu, Z. Sun, and X. H. Chen, Tuning electronic properties of $FeSe_{0.5}Te_{0.5}$ thin flakes using a solid ion conductor field-effect transistor, Phys. Rev. B **95**, 174513 (2017).

[16] J. Shiogai, Y. Ito, T. Mitsuhashi, T. Nojima, and A. Tsukazaki, Electric-field-induced superconductivity in electrochemically etched ultrathin FeSe films on $SrTiO_3$ and MgO, Nat. Phys. **12**, 42 (2016).

[17] B. Lei, J. Cui, Z. Xiang, C. Shang, N. Wang, G. Ye, X. Luo, T. Wu, Z. Sun, and X. Chen, Evolution of High-Temperature Superconductivity from a Low-T_c Phase Tuned by Carrier Concentration in FeSe Thin Flakes, Phys. Rev. Lett. **116**, 077002 (2016).

[18] K. Hanzawa, H. Sato, H. Hiramatsu, T. Kamiya, and H. Hosono, Electric field-induced superconducting transition of insulating FeSe thin film at 35 K, Proc. Natl. Acad. Sci. USA **113**, 3986 (2016).

[19] T. Miyakawa, J. Shiogai, S. Shimizu, M. Matsumoto, Y. Ito, T. Harada, K. Fujiwara, T. Nojima, Y. Itoh, T. Aida, Y. Iwasa, and A. Tsukazaki, Enhancement of superconducting transition temperature in FeSe electric-double-layer transistor with multivalent ionic liquids, Phys. Rev. Mater. **2**, 031801(R) (2018).

[20] S. Kouno, Y. Sato, Y. Katayama, A. Ichinose, D. Asami, F. Nabeshima, Y. Imai, A. Maeda, and K. Ueno, Superconductivity at 38 K at an electrochemical interface between an ionic liquid and $FeSe_{0.8}Te_{0.2}$ on various substrates, Sci. Rep. **8**, 14731 (2018).

[21] E. Piatti, T. Hatano, D. Daghero, F. Galanti, C. Gerbaldi, S. Guastella, C. Portesi, I. Nakamura, R. Fujimoto, K. Iida, H. Ikuta, and R. S. Gonnelli, Ambipolar suppression of superconductivity by ionic gating in optimally doped $BaFe_2(As, P)_2$ ultrathin films, Phys. Rev. Mater. **3**, 044801 (2019).

[22] K. Ueno, H. Shimotani, H. Yuan, J. Ye, M. Kawasaki, and Y. Iwasa, Field-induced superconductivity in electric double layer transistors, J. Phys. Soc. Jpn. **83**, 032001 (2014).

[23] T. Fujimoto and K. Awaga, Electric-double-layer field-effect transistors with ionic liquids, Phys. Chem. Chem. Phys. **15**, 8983 (2013).

[24] P. Gallagher, M. Lee, T. A. Petach, S. W. Stanwyck, J. R. Williams, K. Watanabe, T. Taniguchi, and D. Goldhaber-Gordon, A high-mobility electronic system at an electrolyte-gated oxide surface, Nat. Commun. **6**, 6437 (2015).

[25] E. Piatti, S. Galasso, M. Tortello, J. R. Nair, C. Gerbaldi, M. Bruna, S. Borini, D. Daghero, and R. S. Gonnelli, Carrier mobility and scattering lifetime in electric double-layer gated few-layer graphene, Appl. Surf. Sci. **395**, 37 (2017).

[26] Y. Saito and Y. Iwasa, Ambipolar insulator-to-metal transition in black phosphorus by ionic-liquid gating, ACS Nano **9**, 3192 (2015).

[27] R. S. Gonnelli, E. Piatti, A. Sola, M. Tortello, F. Dolcini, S. Galasso, J. R. Nair, C. Gerbaldi, E. Cappelluti, M. Bruna, and A. C. Ferrari, Weak localization in electric-double-layer gated few-layer graphene, 2D Mater. **4**, 035006 (2017).

[28] E. Piatti, D. De Fazio, D. Daghero, S. R. Tamalampudi, D. Yoon, A. C. Ferrari, and R. S. Gonnelli, Multi-valley superconductivity in ion-gated MoS_2 layers, Nano Lett. **18**, 4821 (2018).

[29] D. Ovchinnikov, F. Gargiulo, A. Allain, D. J. Pasquier, D. Dumcenco, C.-H. Ho, O. V. Yazyev, and A. Kis, Disorder engineering and conductivity dome in ReS_2 with electrolyte gating, Nat. Commun. **7**, 12391 (2016).

[30] E. Piatti, F. Galanti, G. Pippione, A. Pasquarelli, and R. S. Gonnelli, Towards the insulator-to-metal transition at the surface of ion-gated nanocrystalline diamond films, Eur. Phys. J. Spec. Top. **228**, 689 (2019).

[31] J. Lu, O. Zheliuk, Q. Chen, I. Leermakers, N. E. Hussey, U. Zeitler, and J. Ye, Full superconducting dome of strong ising protection in gated monolayer WS_2, Proc. Natl. Acad. Sci. USA **115**, 3551 (2017).

[32] E. Piatti, A. Pasquarelli, and R. S. Gonnelli, Orientation-dependent electric transport and band filling in hole co-doped epitaxial diamond films, Appl. Surf. Sci. **528**, 146795 (2020).

[33] S. Zhang, M.-R. Gao, H.-Y. Fu, X.-M. Wang, Z.-A. Ren, and G.-F. Chen, Electric field induced permanent superconductivity in layered metal nitride chlorides HfNCl and ZrNCl, Chin. Phys. Lett. **35**, 097401 (2018).

[34] X. Wang, S. Zhang, H. Fu, M. Gao, Z. Ren, and G. Chen, Dominant role of processing temperature in electric field induced superconductivity in layered ZrNBr, New J. Phys. **21**, 023002 (2019).

[35] D. Zakhidov, D. A. Rehn, E. J. Reed, and A. Salleo, Reversible electrochemical phase change in monolayer to bulk-like $MoTe_2$ by ionic liquid gating, ACS Nano **14**, 2894 (2020).

[36] Y. Yu, F. Yang, X. F. Lu, Y. J. Yan, Y.-H. Cho, L. Ma, X. Niu, S. Kim, Y.-W. Son, D. Feng, S. Li, S.-W. Cheong, X. H. Chen, and Y. Zhang, Gate-tunable phase transitions in thin flakes of 1T-TaS_2, Nat. Nanotechnol. **10**, 270 (2015).

[37] W. Shi, J. Ye, Y. Zhang, R. Suzuki, M. Yoshida, J. Miyazaki, N. Inoue, Y. Saito, and Y. Iwasa, Superconductivity series in transition metal dichalcogenides by ionic gating, Sci. Rep. **5**, 12534 (2015).

[38] E. Piatti, Q. Chen, and J. Ye, Strong dopant dependence of electric transport in ion-gated MoS_2, Appl. Phys. Lett. **111**, 013106 (2017).

[39] E. Piatti, Q. Chen, M. Tortello, J. Ye, and R. S. Gonnelli, Possible charge-density-wave signatures in the anomalous resistivity of li-intercalated multilayer MoS_2, Appl. Surf. Sci. **461**, 269 (2018).

[40] B. Lei, Z. Xiang, X. Lu, N. Wang, J. Chang, C. Shang, A. Zhang, Q. Zhang, X. Luo, T. Wu, Z. Sun, and X. H. Chen, Gate-tuned superconductor-insulator transition in (Li, Fe)OHFeSe, Phys. Rev. B **93**, 060501(R) (2016).

[41] B. Lei, N. Wang, C. Shang, F. Meng, L. Ma, X. Luo, T. Wu, Z. Sun, Y. Wang, Z. Jiang, B. H. Mao, Z. Liu, Y. J. Yu, Y. B. Zhang, and X. H. Chen, Tuning phase transitions in FeSe thin flakes by field-effect transistor with solid ion conductor as the gate dielectric, Phys. Rev. B **95**, 020503(R) (2017).

[42] Y. Wu, H. Lian, J. He, J. Liu, S. Wang, H. Xing, Z. Mao, and Y. Liu, Lithium ion intercalation in thin crystals of hexagonal $TaSe_2$ gated by a polymer electrolyte, Appl. Phys. Lett. **112**, 023502 (2018).

[43] D. Kwabena Bediako, M. Rezaee, H. Yoo, D. T. Larson, S. F. Zhao, T. Taniguchi, K. Watanabe, T. L. Brower-Thomas, E. Kaxiras, and P. Kim, Heterointerface effects in the electrointercalation of van der Waals heterostructures, Nature **558**, 425 (2018).

[44] X. Che, Y. Deng, Y. Fang, J. Pan, Y. Yu, and F. Huang, Gate-tunable electrical transport in thin 2M-WS_2 flakes, Adv. Electron. Mater. **5**, 1900462 (2019).

[45] C. Shang, B. Lei, W. Zhuo, Q. Zhang, C. Zhu, J. Cui, X. Luo, N. Wang, F. Meng, L. Ma, C. G. Zeng, T. Wu, Z. Sun, F. Q. Huang, and X. H. Chen, Structural and electronic phase transitions driven by electric field in metastable MoS_2 thin flakes, Phys. Rev. B **100**, 020508(R) (2019).

[46] Y. Song, X. Liang, J. Guo, J. Deng, G. Gao, and X. Chen, Superconductivity in Li-intercalated 1T-$SnSe_2$ driven by electric field gating, Phys. Rev. Mater. **3**, 054804 (2019).

[47] N. Lu *et al.*, Electric-field control of tri-state phase transformation with a selective dual-ion switch, Nature **546**, 124 (2017).

[48] X. Leng, J. Pereiro, J. Strle, G. Dubuis, A. Bollinger, A. Gozar, J. Wu, N. Litombe, C. Panagopoulos, D. Pavuna, and I. Božović, Insulator to metal transition in WO_3 induced by electrolyte gating, Npj Quant. Mater. **2**, 35 (2017).

[49] Y. Cui, G. Zhang, H. Li, H. Lin, X. Zhu, H.-H. Wen, G. Wang, J. Sun, M. Ma, Y. Li, D. Gong, T. Xie, Y. Gu, S. Li, H. Luo, P. Yu, and W. Yu, Protonation induced high-T_c phases in iron-based superconductors evidenced by NMR and magnetization measurements, Sci. Bull. **63**, 11 (2018).

[50] M. Rafique, Z. Feng, Z. Lin, X. Wei, M. Liao, D. Zhang, K. Jin, and Q.-K. Xue, Ionic liquid gating induced protonation of electron-doped cuprate superconductors, Nano Lett. **19**, 7775 (2019).

[51] Y. Cui, Z. Hu, J.-S. Zhang, W.-L. Ma, M.-W. Ma, Z. Ma, C. Wang, J.-Q. Yan, J.-P. Sun, J.-G. Cheng, S. Jia, Y. Li, J.-S. Wen, H.-C. Lei, P. Yu, W. Ji, and W.-Q. Yu, Ionic-liquid-gating induced protonation and superconductivity in FeSe, $FeSe_{0.93}S_{0.07}$, ZrNCl, 1T-TaS_2 and Bi_2Se_3, Chin. Phys. Lett. **36**, 077401 (2019).

[52] Z. Li, S. Shen, Z. Tian, K. Hwangbo, M. Wang, Y. Wang, F. M. Bartram, L. He, Y. Lyu, Y. Dong, G. Wan, H. Li, N.

Lu, J. Zang, H. Zhou, E. Arenholz, Q. He, L. Yang, W. Luo, and P. Yu, Reversible manipulation of the magnetic state in $SrRuO_3$ through electric-field controlled proton evolution, Nat. Commun. **11**, 184 (2020).

[53] Y. Meng, X. Xing, X. Yi, B. Li, N. Zhou, M. Li, Y. Zhang, W. Wei, J. Feng, K. Terashima, Y. Takano, Y. Sun, and Z. Shi, Protonation-induced discrete superconducting phases in bulk FeSe single crystals, Phys. Rev. B **105**, 134506 (2022).

[54] E. Piatti, G. Prando, M. Meinero, C. Tresca, M. Putti, S. Roddaro, G. Lamura, T. Shiroka, P. Carretta, G. Profeta, D. Daghero, and R. S. Gonnelli, Coexisting superconductivity and charge-density wave in hydrogen-doped titanium diselenide via ionic liquid gating-induced protonation, arXiv:2205.12951.

[55] J. Jeong, N. Aetukuri, T. Graf, T. D. Schladt, M. G. Samant, and S. S. Parkin, Suppression of metal-insulator transition in VO_2 by electric field–induced oxygen vacancy formation, Science **339**, 1402 (2013).

[56] T. D. Schladt, T. Graf, N. B. Aetukuri, M. Li, A. Fantini, X. Jiang, M. G. Samant, and S. S. Parkin, Crystal-facet-dependent metallization in electrolyte-gated rutile TiO_2 single crystals, ACS Nano **7**, 8074 (2013).

[57] T. A. Petach, M. Lee, R. C. Davis, A. Mehta, and D. Goldhaber-Gordon, Mechanism for the large conductance modulation in electrolyte-gated thin gold films, Phys. Rev. B **90**, 081108(R) (2014).

[58] S. Maruyama, J. Shin, X. Zhang, R. Suchoski, S. Yasui, K. Jin, R. Greene, and I. Takeuchi, Reversible electrochemical modulation of the superconducting transition temperature of $LiTi_2O_4$ ultrathin films by ionic liquid gating, Appl. Phys. Lett. **107**, 142602 (2015).

[59] J. Walter, H. Wang, B. Luo, C. D. Frisbie, and C. Leighton, Electrostatic versus electrochemical doping and control of ferromagnetism in ion-gel-gated ultrathin $La_{0.5}Sr_{0.5}CoO_{3-\delta}$, ACS Nano **10**, 7799 (2016).

[60] L. Zhang, S. Zeng, X. Yin, T. C. Asmara, P. Yang, K. Han, Y. Cao, W. Zhou, D. Wan, C. S. Tang, A. Rusydi, Ariando, and T. Venkatesan, The mechanism of electrolyte gating on high-T_c cuprates: The role of oxygen migration and electrostatics, ACS Nano **11**, 9950 (2017).

[61] S. Zeng, X. Yin, T. Herng, K. Han, Z. Huang, L. Zhang, C. Li, W. Zhou, D. Wan, P. Yang, J. Ding, A. T. S. Wee, J. M. D. Coey, T. Venkatesan, A. Rusydi, and Ariando, Oxygen Electromigration and Energy Band Reconstruction Induced by Electrolyte Field Effect at Oxide Interfaces, Phys. Rev. Lett. **121**, 146802 (2018).

[62] M. S. Saleem, B. Cui, C. Song, Y. Sun, Y. Gu, R. Zhang, M. U. Fayaz, X. Zhou, P. Werner, S. S. Parkin, and F. Pan, Electric field control of phase transition and tunable resistive switching in $SrFeO_{2.5}$, ACS Appl. Mater. Interfaces **11**, 6581 (2019).

[63] Y. Zhang, T. Oka, R. Suzuki, J. Ye, and Y. Iwasa, Electrically switchable chiral light-emitting transistor, Science **344**, 725 (2014).

[64] Q. Chen, J. Lu, L. Liang, O. Zheliuk, A. Ali El Yumin, and J. Ye, Continuous low-bias switching of superconductivity in a MoS_2 transistor, Adv. Mater. **30**, 1800399 (2018).

[65] G. De Simoni, F. Paolucci, P. Solinas, E. Strambini, and F. Giazotto, Metallic supercurrent field-effect transistor, Nat. Nanotechnol. **13**, 802 (2018).

[66] F. Paolucci, G. De Simoni, E. Strambini, P. Solinas, and F. Giazotto, Ultra-efficient superconducting Dayem bridge field-effect transistor, Nano Lett. **18**, 4195 (2018).

[67] F. Paolucci, G. De Simoni, P. Solinas, E. Strambini, N. Ligato, P. Virtanen, A. Braggio, and F. Giazotto, Magneto-transport Experiments on Fully Metallic Superconducting Dayem-Bridge Field-Effect Transistors, Phys. Rev. Appl. **11**, 024061 (2019).

[68] F. Paolucci, F. Vischi, G. De Simoni, C. Guarcello, P. Solinas, and F. Giazotto, Field-effect controllable metallic Josephson interferometer, Nano Lett. **19**, 6263 (2019).

[69] J. H. Cho, J. Lee, Y. Xia, B. Kim, Y. He, M. J. Renn, T. P. Lodge, and C. D. Frisbie, Printable ion-gel gate dielectrics for low-voltage polymer thin-film transistors on plastic, Nat. Mater. **7**, 900 (2008).

[70] S.-K. Lee, S. H. Kabir, B. K. Sharma, B. J. Kim, J. H. Cho, and J.-H. Ahn, Photo-patternable ion gel-gated graphene transistors and inverters on plastic, Nanotechnology **25**, 014002 (2014).

[71] E. Piatti, A. Arbab, F. Galanti, T. Carey, L. Anzi, D. Spurling, A. Roy, A. Zhussupbekova, K. A. Patel, J. M. Kim, D. Daghero, R. Sordan, V. Nicolosi, R. S. Gonnelli, and F. Torrisi, Charge transport mechanisms in inkjet-printed thin-film transistors based on two-dimensional materials, Nat. Electron. **4**, 893 (2021).

[72] S. Shimizu, J. Shiogai, N. Takemori, S. Sakai, H. Ikeda, R. Arita, T. Nojima, A. Tsukazaki, and Y. Iwasa, Giant thermoelectric power factor in ultrathin FeSe superconductor, Nat. Commun. **10**, 825 (2019).

[73] W. Huang, Y. Zhang, M. Song, B. Wang, H. Hou, X. Hu, X. Chen, and T. Zhai, Encapsulation strategies on 2D materials for field effect transistors and photodetectors, Chinese Chemical Letters, (to be published 2021).

[74] H. Jo, J.-H. Choi, C.-M. Hyun, S.-Y. Seo, C.-M. Kim, M.-J. Lee, J.-D. Kwon, H.-S. Moon, S.-H. Kwon, and J.-H. Ahn, A hybrid gate dielectrics of ion gel with ultra-thin passivation layer for high-performance transistors based on two-dimensional semiconductor channels, Sci. Rep. **7**, 14194 (2017).

[75] A. E. Dane, A. N. McCaughan, D. Zhu, Q. Zhao, C.-S. Kim, N. Calandri, A. Agarwal, F. Bellei, and K. K. Berggren, Bias sputtered NbN and superconducting nanowire devices, Appl. Phys. Lett. **111**, 122601 (2017).

[76] O. Medeiros, M. Colangelo, I. Charaev, and K. K. Berggren, Measuring thickness in thin NbN films for superconducting devices, J. Vac. Sci. Technol. A **37**, 041501 (2019).

[77] See the Supplemental Material at http://link.aps.org/supplemental/10.1103/PhysRevApplied.18.054023 for a detailed description of the samples and the fabrication process, the full response of an encapsulated ultrathin film to a triangular gate voltage wave, the sheet resistance modulation at low temperatures, the control experiments in nonencapsulated ultrathin films, the parallel-resistor model for the resistance modulation, and additional details on the x-ray photoelectron spectroscopy of encapsulated ultrathin films and on the measurement and fitting of the tunnelling $V(I)$ curves.

[78] Y. Zhou and S. Ramanathan, Relaxation dynamics of ionic liquid-VO_2 interfaces and influence in electric double-layer transistors, J. Appl. Phys. **111**, 084508 (2012).

[79] F. Scholtz, *Electroanalytical Methods* (Springer-Verlag, Berlin Heidelberg, 2010).

[80] A. Pignolet, G. M. Rao, and S. B. Krupanidhi, Rapid thermal processed thin films of niobium pentoxide (Nb_2O_5) deposited by reactive magnetron sputtering, Thin Solid Films **261**, 18 (1995).

[81] K. Fuchs, The conductivity of thin metallic films according to the electron theory of metals, Math. Proc. Camb. Philos. Soc. **34**, 100 108 (1938).

[82] S. P. Chockalingam, M. Chand, J. Jesudasan, V. Tripathi, and P. Raychaudhuri, Superconducting properties and Hall effect of epitaxial NbN thin films, Phys. Rev. B **77**, 214503 (2008).

[83] T. S. El-Shazly, W. M. Hassan, S. S. Abd-el Rehim, and N. K. Allam, Optical and electronic properties of niobium oxynitrides with various N/O ratios: Insights from first-principles calculations, J. Photonics Energy **8**, 026501 (2018).

[84] G. A. Ummarino, E. Piatti, D. Daghero, R. S. Gonnelli, I. Y. Sklyadneva, E. V. Chulkov, and R. Heid, Proximity Eliashberg theory of electrostatic field-effect doping in superconducting films, Phys. Rev. B **96**, 064509 (2017).

[85] G. A. Ummarino and D. Romanin, Theoretical explanation of electric field-induced superconductive critical temperature shifts in indium thin films, Phys. Status Solidi B **257**, 1900651 (2020).

[86] E. Piatti, D. Romanin, R. S. Gonnelli, and D. Daghero, Anomalous screening of an electrostatic field at the surface of niobium nitride, Appl. Surf. Sci. **461**, 17 (2018).

[87] I. Charaev, T. Silbernagel, B. Bachowsky, A. Kuzmin, S. Doerner, K. Ilin, A. Semenov, D. Roditchev, D. Y. Vodolazov, and M. Siegel, Enhancement of superconductivity in NbN nanowires by negative electron-beam lithography with positive resist, J. Appl. Phys. **122**, 083901 (2017).

[88] M. K. Neylon, S. K. Bej, C. A. Bennett, and L. T. Thompson, Ethanol amination catalysis over early transition metal nitrides, Appl. Catal. A - Gen. **232**, 13 (2002).

[89] A. Ermolieff, M. Girard, C. Raoul, C. Bertrand, and T. M. Duc, An XPS comparative study on thermal oxide barrier formation on Nb and NbN thin films, Appl. Surf. Sci. **21**, 65 (1985).

[90] Z. Lan, H. Fu, R. Zhao, H. Liu, W. Zhou, H. Ning, and J. Guo, Roles of in situ-formed NbN and Nb_2O_5 from N-doped Nb_2C MXene in regulating the re/hydrogenation and cycling performance of magnesium hydride, Chem. Eng. J. **431**, 133985 (2022).

[91] A. Darlinski and J. Halbritter, Angle-resolved XPS studies of oxides at NbN, NbC, and Nb surfaces, Surf. Interface Anal. **10**, 223 (1987).

[92] J. G. Simmons, Generalized formula for the electric tunnel effect between similar electrodes separated by a thin insulating film, J. Appl. Phys. **34**, 1793 (1963).